Article

Structure and Transport Properties in the Pseudobinary Phase System Li$_4$SiS$_4$–Li$_4$SnS$_4$

Lucas G. Balzat, Yan Li, Sascha Dums, Igor Moudrakovski, Kristina Gjorgjevikj, Armin Schulz, Yuheng Li, Simon Krause, Pieremanuele Canepa,* and Bettina V. Lotsch*

ACCESS | 📊 Metrics & More | 📰 Article Recommendations | 🆘 Supporting Information

ABSTRACT: Thio-lithium superionic conductors (thio-LISICONs) are a family of promising solid electrolyte materials for potential applications in solid-state batteries. The orthorhombic polymorph of the thio-LISICON Li$_4$SiS$_4$ (o-Li$_4$SiS$_4$) has been known for decades, but its complete crystal structure has been reported only recently. Here, using single-crystal X-ray diffraction, we reevaluated the crystal structure of o-Li$_4$SiS$_4$ and showed that o-Li$_4$SiS$_4$ crystallizes in space group $Pmn2_1$ (no. 31, a = 7.7694(15) Å, b = 13.731(3) Å, and c = 6.1413(12) Å). The crystal structure of o-Li$_4$SiS$_4$ consists of isolated SiS$_4$ tetrahedra arranged in a zigzag-type manner, whereas Li atoms are coordinated both tetrahedrally and octahedrally by sulfur atoms of the SiS$_4$ groups. Structures identified by first-principles calculations support the lower symmetry solution presented here, with the $Pmn2_1$ polymorph being more stable at room temperature than a higher symmetry phase. By knowing the accurate crystal structure of o-Li$_4$SiS$_4$, we investigated the solid solution behavior with another group IV thio-LISICON, Li$_4$SnS$_4$. Rietveld refinements of powder X-ray diffraction data revealed the solid solution Li$_4$Si$_{1−x}$Sn$_x$S$_4$ ($0 \le x \le 1$, $\Delta x = 0.1$), which shows a nearly ideal Vegard-type behavior for all silicon-containing samples. ^{29}Si and ^{119}Sn magic-angle-spinning solid-state NMR and Raman spectroscopy showed the presence of SiS$_4$ and SnS$_4$ tetrahedral moieties, with the spectra showing expected behavior consistent with the silicon−tin ratio in the materials. Electrochemical impedance spectroscopy revealed the highest ionic conductivity of 8.4×10^{-6} S cm^{-1} at 25 °C for Li$_4$Si$_{0.5}$Sn$_{0.5}$S$_4$, accompanied by the lowest migration barrier of ∼0.37 eV.
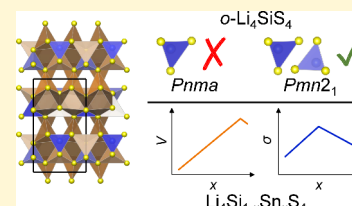
INTRODUCTION

Lithium ion solid electrolytes (Li-SEs) have garnered a lot of attention due to their potential use in solid-state batteries (SSBs), which promise high power- and energy densities, in addition to safety improvements when compared to conventional liquid electrolyte-based lithium-ion batteries.[1,2] Among Li-SEs, sulfide Li-SEs are of particular interest due to generally higher ionic conductivities and better mechanical properties for easier processing.[3] Some sulfide Li-SEs, such as Li$_{10}$GeP$_2$S$_{12}$ (LGPS, 1.2×10^{-2} S cm^{-1}),[4] Li$_{5.5}$PS$_{4.5}$Cl$_{1.5}$ (9.4×10^{-3} S cm^{-1}),[5] Li$_{9.54}$Si$_{1.74}$P$_{1.44}$S$_{11.7}$Cl$_{0.3}$ (2.5×10^{-2} S cm^{-1}),[6] or Li$_{9.54}$(Si$_{0.6}$Ge$_{0.4}$)$_{1.74}$P$_{1.44}$S$_{11.1}$Br$_{0.3}$O$_{0.6}$ (3.2×10^{-2} S cm^{-1})[7] exhibit room temperature (RT) ionic conductivities rivaling or even exceeding the ionic conductivities of liquid electrolytes used in conventional lithium-ion batteries (∼1.0×10^{-2} S cm^{-1}).[8] Besides their high ionic conductivities, SEs also need to be cost-effective. This prevents SEs, such as LGPS and some of its derivatives from widespread application in SSBs, because they contain expensive and scarce elements, primarily germanium.[3,9]

In search for SEs, containing more abundant and sustainable elements, one may look toward the family of thio-lithium ion superionic conductors (thio-LISICONs). In general, thio-LISICONs were developed from the oxide-based family of LISICONs.[10,11] Kanno et al. were first to replace the hard and small O^{2-} ion with the more polarizable and larger S^{2-}, thus

achieving a significant increase in RT Li-ion conductivity of these materials.[12,13] The crystal structures of thio-LISICONs are generally related to the Li$_4$SiO$_4$ or γ-Li$_3$PO$_4$ structure types featuring a hexagonal close packing of sulfur and an arrangement of MS$_4$ tetrahedra (with M = Al, Si, Ge, Sn, P, As, Sb).[3,11,14,15] Examples for ternary thio-LISICONs with a Li$_4$SiO$_4$- or γ-Li$_3$PO$_4$-related structure include, among others, Li$_4$SiS$_4$,[16,17] Li$_4$GeS$_4$,[18,19] Li$_4$SnS$_4$,[20,21] and β-Li$_3$PS$_4$.[22,23]

Li$_4$SiS$_4$, a SE, which contains readily available and highly abundant silicon,[9] has been known since 1989, but still remains poorly characterized. Two polymorphs of Li$_4$SiS$_4$ exist, an orthorhombic (o-Li$_4$SiS$_4$) and a monoclinic (m-Li$_4$SiS$_4$) one, yet the reported crystal structures of both polymorphs appear incomplete. o-Li$_4$SiS$_4$ was first synthesized and described by Ahn and Huggins. Using data from powder X-ray diffraction (PXRD) they indexed the structure with an orthorhombic unit cell ($Pnma$, no. 62) without reporting atomic positions.[16] m-Li$_4$SiS$_4$ with a monoclinic unit cell ($P2_1/m$, no. 11) was reported by Murayama et al. in 2002. However, only the

A

atomic positions for silicon and sulfur were provided.[17] Recently, utilizing combined Rietveld refinements of PXRD and powder neutron diffraction data, Roh et al. reported the full crystal structures of both Li_4SiS_4 polymorphs.[24] Using the m-Li_4SiS_4[17] and Li_4GeS_4 ($Pnma$, no. 62)[19] structures as starting models, they obtained lattice parameters, which are in good agreement with the previously reported lattice parameters of both o-Li_4SiS_4 and m-Li_4SiS_4. o-Li_4SiS_4 and m-Li_4SiS_4 were also indexed with the same space groups as reported previously, $Pnma$ and $P2_1/m$, respectively.[17,24] Despite achieving good refinements with satisfactory R factors, the occupancies of some lithium positions had to be fixed to not exceed their maximum occupancies during refinement.[24]

Here, using single crystal X-ray diffraction (SXRD), we propose an updated crystal structure of o-Li_4SiS_4, which crystallizes with a lower symmetry in the noncentrosymmetric space group $Pmn2_1$ (no. 31) with fully occupied atomic positions. The structure of o-Li_4SiS_4 was further corroborated using ^{29}Si MAS NMR, Raman spectroscopy, and first-principles simulations.

Besides a high ionic conductivity, other properties of SEs, for example, their environmental stability, are important for the commercialization in SSBs. The thio-LISICON Li_4SnS_4 has been thoroughly investigated because of its moisture stability, since Li_4SnS_4 tends to form hydrates first before releasing H_2S due to hydrolysis.[25−29] In order to potentially increase the environmental stability of o-Li_4SiS_4, we also report the isovalent substitution of o-Li_4SiS_4 with tin in the solid solution series $Li_4Si_{1−x}Sn_xS_4$ ($0 \leq x \leq 1$, $\Delta x = 0.1$). Tin was chosen since it is a relatively abundant metal, and may improve the ionic conductivity and environmental stability of $Li_4Si_{1−x}Sn_xS_4$ SEs.[9] Through Rietveld refinements, we show that $Li_4Si_{1−x}Sn_xS_4$ exhibits a nearly ideal Vegard behavior. The local structure was investigated using ^{29}Si and ^{119}Sn MAS NMR and Raman spectroscopy. Raman measurements were further confirmed by first-principles simulations. Finally, using electrochemical impedance spectroscopy we report the Li-ion transport properties, showing that with a 1:1 Si to Sn ratio ($x = 0.5$) an average ionic conductivity of 8.4×10^{-6} S cm^{-1} at 25 °C is obtained, which is more than twice what was obtained for o-Li_4SiS_4 (1.5×10^{-6} S cm^{-1}) and Li_4SnS_4 (3.7×10^{-6} S cm^{-1}).

■ EXPERIMENTAL PROCEDURE

Synthesis of Members of the $Li_4Si_{1−x}Sn_xS_4$ Solid Solution. Members of the $Li_4Si_{1−x}Sn_xS_4$ solid solution were synthesized by grinding appropriate stoichiometric amounts of Li_2S (Sigma-Aldrich, 99.98%), Si (Alfa Aesar, 99.99%), Sn (Sigma-Aldrich, 99.8%), and S (Grüssing) in an agate mortar. Sulfur was resublimed under vacuum prior to use, all other chemicals were used without further purification. An excess of sulfur (5 wt %) was added to all samples to counter sulfur loss due to sublimation and to ensure full oxidation of Si and Sn to +IV. The ground starting materials were then transferred into glassy carbon crucibles and subsequently sealed in evacuated silica ampules. Prior to use the ampules were heated under vacuum using a hydrogen torch in order to remove surface water. A tubular furnace was used to heat the ampules to 525 °C with a rate of 50 °C h^{-1}. The ampules were kept at 525 °C for 100 h before switching off the furnace and letting them cool down naturally. This temperature program was chosen since it resulted in the formation of o-Li_4SiS_4 over m-Li_4SiS_4 and yielded samples with high phase purity. o-Li_4SiS_4 single crystals were selected from a sample that was heated up to 600 °C with a rate of 50 °C h^{-1} and held there for 72 h before the furnace was turned off and the sample was allowed to cool naturally.

All members of the $Li_4Si_{1−x}Sn_xS_4$ solid solution were obtained as moisture-sensitive, yellowish solids. All chemicals and products were handled under inert conditions in an argon-filled glovebox (MBraun, $O_2 < 0.1$ ppm, $H_2O < 1$ ppm) or in argon-filled containers at all times.

Single-Crystal X-ray Diffraction of o-Li_4SiS_4. Single crystals of o-Li_4SiS_4 were isolated under paraffin oil (dried with potassium metal) and sealed in glass capillaries (Hilgenberg) under oil. Measurements were carried out with a Bruker D8 Quest diffractometer using Mo−K_α radiation ($\lambda = 0.71073$ Å). Data handling, including a multiscan absorption correction with the program SADABS, was done utilizing the Bruker Apex 3 software package.[30] The structure solution and inversion twin refinement were performed with the programs SHELXS-97 and SHELXL2019/2, respectively.[31] Crystal structure drawings were produced using VESTA3.[32]

Powder X-ray Diffraction. Powder X-ray diffraction (PXRD) was carried out using a Stoe Stadi P powder diffractometer (Ge(111) monochromator, Dectris MYTHENII K detector) in Debye−Scherrer geometry using Ag $K_{\alpha1}$ radiation ($\lambda = 0.55942$ Å). All samples were flame-sealed in glass capillaries (Hilgenberg) with a diameter of 0.5 mm. Rietveld refinements were performed using the software TOPAS 6 (Bruker).[33] During refinements the lattice parameters, the isotropic temperature parameters, atomic positions, the mixed occupation of Si1 and Si2 positions with tin, and stress and strain were refined. No penalties or restraints were used during refinements. Due to the low X-ray scattering cross section of Li$^+$ no refinements of lithium atoms were performed.

Solid-State NMR. Solid-state magic-angle-spinning (MAS) NMR was performed on a Bruker Avance III 400 MHz instrument at a magnetic field of $B_0 = 9.4$ T. MAS NMR experiments were carried out in 4 mm OD ZrO_2 rotors at a spinning frequency of 10 kHz using a Bruker BL4 WVT double-channel probe. ^{29}Si and ^{119}Sn direct excitation spectra were acquired using $\pi/4$ RF pulses (3 and 2 μs) in 2000 and 32 scans and recycle delays of 20 and 120 s, respectively. The chosen relaxation delays were long enough for a complete relaxation of all signals. Chemical shifts were externally referenced to tetramethyl silane (^{29}Si $\delta_{iso} = 0.0$ ppm) and SnO_2 (^{119}Sn $\delta_{iso} = -603.0$ ppm). The temperature in the probe was regulated with a Bruker BVT3000 temperature controller. Actual temperature inside the rotor was calibrated on the ^{207}Pb signal of powdered $Pb(NO_3)_2$.[34]

Raman Spectroscopy. Raman spectroscopy was carried out on samples in the same capillaries used for PXRD analysis. Raman spectra were recorded on a home-build system comprising a 785 nm laser equipped with a Raman Probe (Coherent TR-Probe 300 mW power at sample port, a steerable noncontact optic and a flood light module as accessories) and connected to a spectrograph (Andor Kymera 328i, Andor iDUS 420 CCD detector). Measurements were done at 30% laser power on the sample and at ambient temperature.

Scanning Electron Microscopy and Energy-Dispersive X-ray Spectroscopy. Scanning electron microscopy (SEM) and energy-dispersive X-ray spectroscopy (EDS) were performed in a Zeiss Merlin electron microscope. For EDS either an Oxford Instruments Ultim Max or an Oxford Instruments Ultim Extreme EDS detector was used. All samples were not sputtered and had brief contact with air during transfer into the electron microscope.

Electrochemical Measurements. For electrochemical impedance spectroscopy (EIS) measurements all samples were ground in agate mortars and compacted into pellets using uniaxial cold pressing with a pelletizing pressure of ∼1 GPa. All pellets had a diameter of 5 mm, a thickness ranging between 0.3 and 1.4 mm and relative densities between 75 and 95% with an average density of 89%. The pellets were loaded into RHD Instruments TSC SW closed measurement cells. The pressure applied in the measurement cells was ∼650 kPa. The conditions for sample preparation were chosen, since, from our experience, they lead to good quality data for mechanically soft sulfide Li-SEs. The measurement cells were connected to a RHD Instruments Microcell HC measuring stand. EIS spectra were recorded using an Ivium CompactStat.h potentiostat between 1 MHz-0.1 Hz and with an excitation voltage of 100 mV. Impedances Z were normalized by multiplying Z with the quotient of the pellet surface area A and the pellet thickness d. To determine the

activation energy E_a, temperature-dependent EIS measurements between 25 and 75 °C in 5 °C steps and an equilibration time of 1 h were carried out. E_a was obtained by fitting the temperature-dependent data to a modified Arrhenius-type equation of the form $\sigma T = \sigma_0 e^{(-E_a/k_B T)}$ using the ionic conductivity σ, the temperature T, the pre-exponential factor σ_0 and the Boltzmann constant k_B.[35] Data handling, processing and fitting procedures were carried out using the software RelaxIS3 (RHD Instruments). Based on the recommendations by Ohno et al., EIS measurements were carried out on three different samples with the obtained conductivities and activation energies averaged in order to gain more reliable data.[36]

Computational Methods. First-principles calculations based on Density Functional Theory (DFT)[37] were performed using the Vienna Ab initio Simulation Package (VASP).[38,39] The exchange-correlation interactions were approximated with the r^{2}SCAN functional.[40] This meta-generalized gradient approximation offers enhanced numerical stability and computational efficiency compared to its predecessor, SCAN.[41,42] Core electrons were described using the projector augmented wave (PAW) method,[43] while valence electrons were represented explicitly using a plane-waves basis set with a kinetic energy cutoff of 520 eV. The PAW potentials used include: Li$_{sv}$ 10Sep2004 1s^{2}2s^1, Si 05Jan2001 3s^{2}3p^2, Sn$_d$ 06Sep2000 1s^{2}1p^2, and S 06Sep2000 3s^{2}3p^4. Each structure was fully optimized (including atomic positions, cell shape, and volume) using a Γ-centered Monkhorst–Pack k-point mesh with a spacing of ≤ 0.5 Å^{-1} to sample the Brillouin zone. The convergence threshold for DFT total energy changes was set to 10^{-5} eV/cell, and forces on atoms were converged to within 10^{-2} eV/Å.

Phonon dispersion, vibrational free energy, and Raman intensities were calculated using the CRYSTAL23 software[44] with DFT and the PBE0 hybrid functional (25% Hartree–Fock exchange),[45] which has demonstrated good agreement with experimental measurements.[46] Self-consistent field (SCF) energies were converged to a threshold of 10^{-11} Hartree (per cell) using a Monkhorst–Pack k-point grid of $8 \times 8 \times 8$. Truncation tolerances for Coulomb integrals (overlap and penetration) and Hartree–Fock exchange integrals were set to 10^{-7} Hartree, with pseudo-overlap thresholds of 10^{-9} and 10^{-30} Hartree. Crystalline orbitals of Li, Si, and S were described by Gaussian triple-ζ valence basis sets with polarization (pob-TZVP-rev2).[47] For Sn, an effective core potential (ECP28MDF) with 14 valence electrons (5s, 5p, and 4d) treated explicitly was adopted to account for relativistic effects common in heavier elements.[48] Phonon dispersions and vibrational free energies were calculated using the CRYSTAL-Phonopy interface within the Phonopy package.[49] These calculations employed $2 \times 1 \times 2$ and $1 \times 2 \times 2$ supercell models (both with 144 atoms) with a single Γ point for the $Pmn2_1$ and $Pnma$ structures of o-Li$_4$SiS$_4$, respectively.

■ RESULTS AND DISCUSSION

Crystal Structure of Li$_4$Si$_{1-x}$Sn$_x$S$_4$ (x = 0.0): o-Li$_4$SiS$_4$. Figure 1a,b show the crystal structure of o-Li$_4$SiS$_4$ determined from SXRD. Further crystallographic information is listed in Table 1 and Tables S1 and S2 in the Supporting Information. o-Li$_4$SiS$_4$ crystallizes in the orthorhombic space group $Pmn2_1$ (no. 31) with lattice parameters a = 7.7694(15) Å, b = 13.731(3) Å, and c = 6.1413(12) Å.

The structure of o-Li$_4$SiS$_4$ consists of sulfur atoms forming a hexagonal close packing with silicon atoms and lithium atoms occupying 1/2 of the tetrahedral voids and additional lithium atoms occupying 1/4 of the octahedral voids. All crystallographic positions have 100% occupancy. The isolated SiS$_4$ tetrahedra form a distinct zigzag-like arrangement, whose apexes point up and down in an alternating manner, as shown in Figure 1c. The same zigzag structural motif is also found in the PS$_4$ tetrahedra arrangement in orthorhombic β-Li$_3$PS$_4$.[22,23] The Si–S bond lengths in the SiS$_4$ tetrahedra (2.11–2.16 Å) are similar to lengths observed in other SiS$_4$-containing
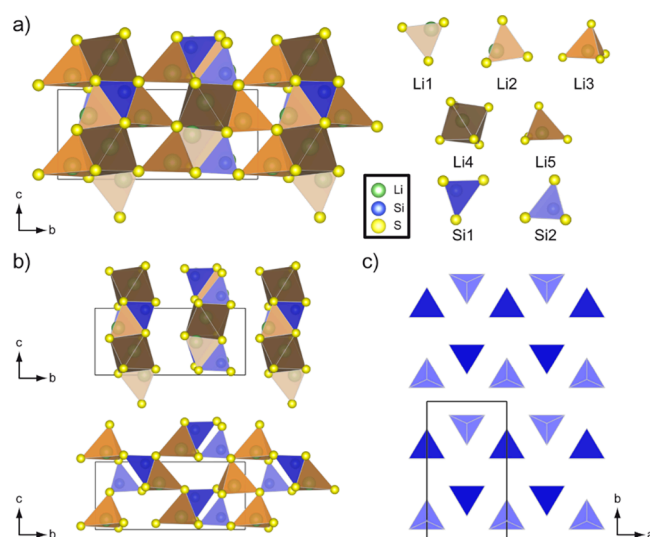

Figure 1. (a) Crystal structure of o-Li$_4$SiS$_4$ and sulfur coordination polyhedra of lithium and silicon. (b) Partial crystal structure of o-Li$_4$SiS$_4$ depicting the stacking of the Li–S polyhedra. (c) Zig-zag arrangement of the SiS$_4^{4-}$ tetrahedra found in o-Li$_4$SiS$_4$. The unit cell is highlighted in all drawings as well.

compounds.[17,50] Lithium atoms are found both in four- and six-fold coordination environments by sulfur atoms. Lithium atoms on the Li4 site form edge-sharing LiS$_6$ octahedra, giving rise to infinite chains along the a-axis. The LiS$_6$ octahedra are distorted with Li–S distances in the range of 2.572(5)–3.292(6) Å. The LiS$_4$ tetrahedra formed by Li3 and Li5 sites stack in an alternating manner along the c-axis via corner-sharing sulfur atoms, while the (Li1)S$_4$ and (Li2)S$_4$ tetrahedra share corners and edges with the SiS$_4$ tetrahedra. All LiS$_4$ tetrahedra appear distorted, with Li–S distances from 2.376(9)–2.627(1) Å, but to a lesser extent than the LiS$_6$ octahedra. The stacking of the lithium polyhedra is visualized in Figure 1b.

To further verify the crystal structure of o-Li$_4$SiS$_4$ we conducted ^{29}Si MAS NMR and Raman measurements. The ^{29}Si MAS NMR spectrum (Figure 2a) shows two singlet signals, one at 8.8 ppm and one at 4.8 ppm. Two singlet signals suggest the presence of two crystallographically distinct Si positions in the crystal structure, supporting the o-Li$_4$SiS$_4$ structure reported here. The chemical shift range of the two signals is also in good agreement with chemical shifts reported for SiS$_4$ units in the literature.[51,52] Eckert et al. reported a similar ^{29}Si MAS NMR spectrum of o-Li$_4$SiS$_4$, but were not able to fully explain their signals due to the absence of full structural data at that time.[53] The experimental Raman spectrum in Figure 2b shows its most intense signal at 394 cm^{-1}, which aligns well with our calculated value of 400 cm^{-1}. Based on several reports of materials containing isolated SiS$_4$ tetrahedra and our Raman simulation results, this signal was assigned to the symmetric stretching vibration of the SiS$_4$ tetrahedron.[54,55] The other signals might be assigned to other vibrational modes of the SiS$_4$ tetrahedron or lattice modes.[56−58] From our DFT calculations, the Raman modes at 92 and 527 cm^{-1} were assigned to the bending and asymmetric stretching modes of the SiS$_4$ tetrahedron, respectively. Details of the calculated Raman data for o-Li$_4$SiS$_4$ are listed in Table S3.

Table 1. Fractional Atomic Coordinates and Equivalent Displacement Parameters of o-Li$_4$SiS$_4$[a]

atom	occupation	Wyckoff position	x	y	z	U_{equiv}
Li1	1	2a	0	0.3279(6)	0.0002(17)	0.032(2)
Li2	1	2a	0	0.8455(6)	0.2069(14)	0.027(2)
Li3	1	4b	0.2517(6)	0.0732(3)	0.1452(9)	0.0275(10)
Li4	1	4b	0.2695(7)	0.2614(3)	0.3622(8)	0.0279(12)
Li5	1	4b	0.2669(6)	0.5737(3)	0.1837(8)	0.0273(10)
Si1	1	2a	0	0.66593(8)	0.47625(17)	0.0111(3)
S1	1	2a	0	0.66407(7)	0.13059(18)	0.0129(2)
S4	1	4b	0.27382(10)	0.40394(6)	0.08972(9)	0.01413(17)
S5	1	2a	0	0.81075(7)	0.60123(17)	0.0128(2)
Si2	1	2a	0	0.16138(8)	0.68043(17)	0.0101(3)
S2	1	2a	0	0.15515(8)	0.02352(18)	0.0155(2)
S3	1	4b	0.22569(9)	0.09610(5)	0.55134(9)	0.01381(17)
S6	1	2a	0	0.31097(7)	0.57430(15)	0.0117(2)

[a]Space group $Pmn2_1$ (no. 31), a = 7.7694(15) Å, b = 13.731(3) Å, c = 6.1413(12) Å, V = 665.2(2) Å^3. Standard deviations are given in parentheses.
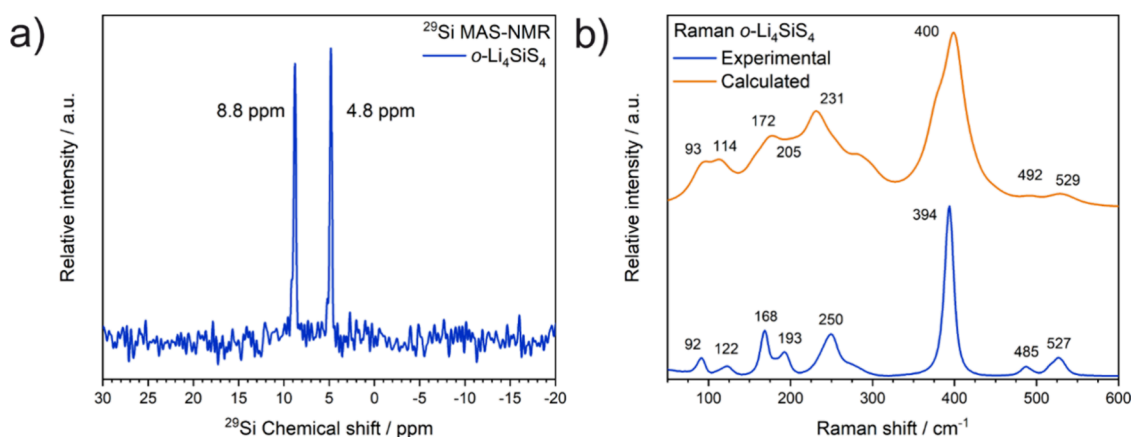

Figure 2. (a) ^{29}Si MAS NMR and (b) experimental (excitation 785 nm) and calculated Raman spectra of o-Li$_4$SiS$_4$. The calculated spectrum was generated by convoluting Raman-active modes from Table S3, with a Lorentzian line shape (fwhm = 15 cm^{-1}) assuming a 785 nm wavelength as used in the experimental measurements.

Recently, Roh et al.[24] reported a complete structure refinement of o-Li$_4$SiS$_4$, who used Rietveld refinements starting from a Li$_4$GeS$_4$ model[19] to determine the structure. The unit cells reported by Roh et al. and in our work here are in good agreement with each other.[24] However, we propose a lower symmetry for o-Li$_4$SiS$_4$ based on several observations, in contrast to Roh et al., who reported the structure in the higher symmetry space group $Pnma$ (no. 62). First, the ^{29}Si MAS NMR discussed earlier (Figure 2) shows two signals, indicating two independent crystallographic Si positions as opposed to only one in the o-Li$_4$SiS$_4$ structure reported by Roh et al.[24] Second, the precession image for the $0kl$ plane (see Figure S1) exhibits additional weak reflections. These additional reflections break the apparent zonal reflection condition ($k + l = 2n$) for the a-glide plane in space group $Pnma$.[59] Upon removing the a-glide plane the overall symmetry is lowered, resulting in the space group $Pmn2_1$ (no. 31).[59−62] Third, the lower space group symmetry allows for resolving the lithium atom disorder in the $Pnma$ structure from Roh et al.,[24] where restraints of lithium occupancies were necessary to avoid exceeding 100% occupancy during refinement. In $Pmn2_1$ more crystallographic positions for lithium to occupy are available, resulting in the absence of lithium vacancy disorder in our structure model.

Since $Pmn2_1$ is a direct subgroup of $Pnma$, a group-subgroup relationship between the Li$_4$GeS$_4$ and the o-Li$_4$SiS$_4$ structure type can be envisioned, which is shown in Figure S2.[19,63,64]

Starting from the coordinates proposed by Roh et al. and applying the necessary symmetry reduction and coordinate transformations leads to the calculated atom coordinates (see Figure S2). We find good agreement between the atom coordinates extracted from the o-Li$_4$SiS$_4$ structures obtained from SXRD with those obtained by transforming the coordinates by Roh et al.[24] This comparison shows the close relationship between the Li$_4$GeS$_4$ and the o-Li$_4$SiS$_4$ structure types (see Table S4).[19,24] An overlay of both structures is shown in Figure S3.

First-principles DFT calculations were performed to confirm the ground state structure of o-Li$_4$SiS$_4$ ($Pmn2_1$ vs $Pnma$).[37] In addition to constructing a $Pmn2_1$ model of o-Li$_4$SiS$_4$ from our experimental data (denoted as o-Li$_4$SiS$_4^i$), we simulated three $Pnma$ o-Li$_4$SiS$_4$ polymorphs to expand the range of structural variations investigated. These polymorphs included: (i) the disordered $Pnma$ o-Li$_4$SiS$_4$ reported by Roh et al.[24] (indicated as o-Li$_4$SiS$_4^{ii}$), (ii) disordered (o-Li$_4$SiS$_4^{iii}$), and (iii) ordered (o-Li$_4$SiS$_4^{iv}$) $Pnma$ structures. The latter two models are hypothetical and were derived by substituting Si for Sn in the analogous disordered and ordered $Pnma$ Li$_4$SnS$_4$ structures, as reported by Kwak et al.[65] and MacNeil et al.,[21] respectively. All models of these structures are summarized in Table S5.

Table S6 summarizes the calculated and measured results for the $Pmn2_1$ o-Li$_4$SiS$_4^i$ structures, showing good agreement of the lattice constants with a relative discrepancy within 0.5%. Given

the presence of Li-site disorder in both o-Li$_4$SiS$_4^{ii}$ and o-Li$_4$SiS$_4^{iii}$, as observed in their experimental structures, ordering of the atomic positions is required to determine the lowest-energy configurations in these systems. Different distributions of the Li-atom fractional occupancy can be envisioned: in o-Li$_4$SiS$_4^{ii}$ (Table S6) three out of the four Li sites exhibit partial occupancy (50%), whereas in the o-Li$_4$SiS$_4^{iii}$ model (in analogy to Li$_4$SnS$_4^i$ in Table S8), two out of four Li sites are partially occupied (25%). Through a systematic enumeration of all symmetrically distinct Li-ordering configurations within the 36-atom conventional cell (four formula units) of each model, we identified 161 and 252 unique ordered model representatives for the o-Li$_4$SiS$_4^{ii}$ and o-Li$_4$SiS$_4^{iii}$ structures, respectively. Subsequent structural optimization with DFT reveals that the most energetically favorable configurations derived from both o-Li$_4$SiS$_4^{ii}$ and o-Li$_4$SiS$_4^{iii}$ models, initially reported as disordered $Pnma$ phases in experimental studies,[24,65] belong in space group $Pmn2_1$. Notably, these two optimized structures exhibit energies nearly identical (within a numerical error of ~10^{-3} meV/atom) to the optimized $Pmn2_1$ o-Li$_4$SiS$_4^i$ structure, i.e. $E(o\text{-Li}_4\text{SiS}_4^i) \equiv E(o\text{-Li}_4\text{SiS}_4^{ii}) \equiv E(o\text{-Li}_4\text{SiS}_4^{iii})$, all in the $Pmn2_1$ space group. Table S6 also lists the results for the o-Li$_4$SiS$_4^{ii}$ structure, indicating that the relaxed $Pmn2_1$ o-Li$_4$SiS$_4^{ii}$ (which initially was solved in $Pnma$) is structurally equivalent to o-Li$_4$SiS$_4^i$ within 10^{-3} of the fractional atomic positions differences. In contrast, the relaxed o-Li$_4$SiS$_4^{iv}$ structure maintains $Pnma$ symmetry, with an energy 4.10 meV/atom higher than the $Pmn2_1$ phase. The close structural similarity between the ground state $Pmn2_1$ and $Pnma$ phases of o-Li$_4$SiS$_4$ (o-Li$_4$SiS$_4^i$ vs o-Li$_4$SiS$_4^{iv}$) is demonstrated in Figure S4. Table S7 compares their lattice parameters and atomic positions, emphasizing the direct group-subgroup relationship between the two phases.[59−62]

Comparison of the simulated X-ray diffraction patterns for different o-Li$_4$SiS$_4$ structural models with the experimentally measured pattern from this work shows the close similarity among $Pmn2_1$ o-Li$_4$SiS$_4^i$ (Figure 3a,b), o-Li$_4$SiS$_4^{ii}$ (Figure 3c), and o-Li$_4$SiS$_4^{iii}$ (Figure 3d) phases. In contrast, the simulated pattern for $Pnma$ o-Li$_4$SiS$_4^{iv}$ (Figure 3e) exhibits a mismatch in several reflection positions (as highlighted in the gray regions)

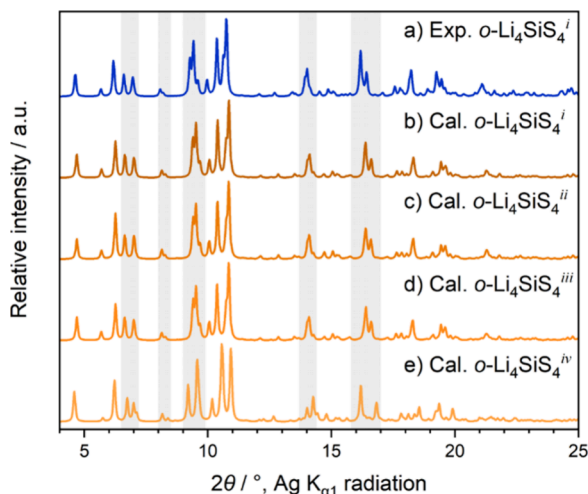**Figure 3.** Comparison of the (a) experimental diffraction pattern of o-Li$_4$SiS$_4$ with (b−e) simulated diffraction patterns derived from the DFT models of o-Li$_4$SiS$_4$. Gray regions highlight discrepancies between the different patterns.

when compared to other polymorphs and experimental results. For example, at $2\theta \approx 14°$, the o-Li$_4$SiS$_4^{iv}$ structure displays two reflections, unlike the overlapping reflections observed in the other patterns. Such reflection overlap can be attributed to the group-subgroup relationship between the $Pnma$ and $Pmn2_1$ spacegroups.[59−62]

To assess the effects of lattice vibrations to the thermodynamic stability of the $Pmn2_1$ and $Pnma$ phases of o-Li$_4$SiS$_4$, we first examined their dynamical stability through phonon dispersion calculations (Figures S5 and S6). The absence of imaginary frequencies indicates that both phases are dynamically stable. Their phonon frequencies span a similar range in both structures, with an upper limit of approximately 570 cm^{-1}.

Having established dynamical stability, we evaluated the temperature-dependent Helmholtz free energy F. For crystalline systems with negligible volume changes, F can be approximated as $F = F_{vib} + E$. F_{vib} represents the vibrational free energy, which quantifies the contributions of lattice vibrations to the total free energy and is derived by integrating the phonon density of states over the entire frequency range.[66] E is the DFT total energy of the optimized crystal structure, with $E(Pnma) - E(Pmn2_1) = 4.10$ meV/atom. Figure 4
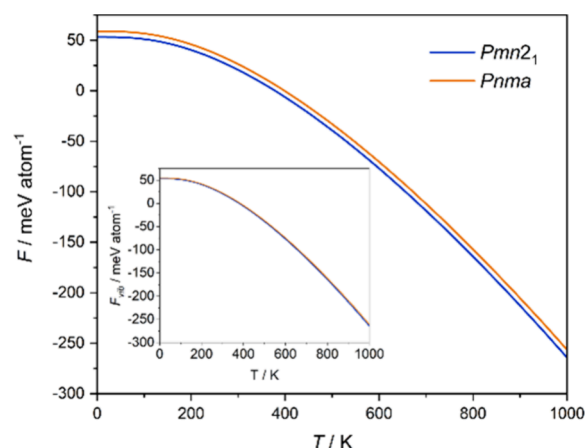

Figure 4. Plot of the DFT computed free energy F for the $Pmn2_1$ and the $Pnma$ polymorphs of o-Li$_4$SiS$_4$ as a function of temperature. The inset shows the vibrational contribution F_{vib}. The static energy of the $Pmn2_1$ phase ($E(Pmn2_1)$) was set to zero as the energy reference.

illustrates F and F_{vib} for $Pmn2_1$ and $Pnma$ o-Li$_4$SiS$_4$ over the temperature range of 0−1000 K. As shown in the inset of Figure 4, the vibrational free energies of the two phases are remarkably similar, with nearly superimposed curves. The difference in total free energy between the two phases is therefore primarily attributed to the difference in their static lattice energies E, with the $Pmn2_1$ phase consistently exhibiting a lower free energy (by ~4.10 meV/atom) than the $Pnma$ phase across the explored temperature range. Given the small free energy difference, the $Pmn2_1$ and $Pnma$ o-Li$_4$SiS$_4$ are expected to coexist at ambient temperature (298 K).

Crystal Structure of Li$_4$Si$_{1-x}$Sn$_x$S$_4$ ($x = 1.0$): Li$_4$SnS$_4$. As previously noted, Li$_4$SnS$_4$ possesses two polymorphs: one with an ordered[21] and one with a disordered[20,65,67] lithium substructure. The structures have been reported by several groups and appear quite similar, all crystallizing in $Pnma$, with the disordered structure having a slightly lower volume (ordered: 715 Å^3;[21]; disordered: 700 Å^3,[20] 706 Å^3,[67] 712

Å^3,[65]), probably due to different lithium packing.[20,21,65,67,68] In this work, the Li$_4$SnS$_4$ PXRD patterns were refined using the disordered structure by Kwak et al.[65] and are in good agreement with lattice parameters reported in the literature (Figure S18 and Table S19).[20,67]

The $Pnma$ and $Pmn2_1$ phases of Li$_4$SnS$_4$ were also investigated computationally. We considered both the experimentally reported disordered model (denoted as Li$_4$SnS$_4^i$ by Kwak et al.[65]) and the ordered structure (Li$_4$SnS$_4^{ii}$ by MacNeil et al.[21]), along with a hypothetical $Pmn2_1$ Li$_4$SnS$_4$ structure (Li$_4$SnS$_4^{iii}$) generated by substituting Si with Sn in the $Pmn2_1$ o-Li$_4$SiS$_4$ (see Table S5). Kaib and co-workers[20] also reported a disordered $Pnma$ structure for Li$_4$SnS$_4$. However, given the high similarity in site positions and occupancies to the Li$_4$SnS$_4^i$ model used in this work, we anticipate nearly identical simulation results. To this end, a systematic computational search of 252 distinct orderings within the 36-atom conventional cell of the disordered Li$_4$SnS$_4^i$ resulted in a lowest-energy configuration. This configuration is isoenergetic with the Li$_4$SnS$_4^{ii}$, such that $E(\text{Li}_4\text{SnS}_4^i) \equiv E(\text{Li}_4\text{SnS}_4^{ii})$, with both structures described by a $Pnma$ symmetry.

Table S8 compares the calculated lattice parameters and atomic coordinates of the $Pnma$ Li$_4$SnS$_4^i$ and Li$_4$SnS$_4^{ii}$ models with their respective experimental measurements.[21,65] This comparison quantitatively supports that both experimental structures converge to the same configuration, exhibiting nearly identical calculated lattice constants and fractional coordinates (differences within 0.001 Å and 0.001, respectively). Specifically, the two 8d Li sites, which exhibit 25% occupancy in the experimental Li$_4$SnS$_4^i$ structure, relaxed to a single fully occupied 4a site in the calculated structure. The X-ray diffraction analysis in Figure S7 shows two reflections in the calculated $Pnma$ Li$_4$SnS$_4^i$ and Li$_4$SnS$_4^{ii}$ (Figure S7b,d), occurring at $2\theta = \sim 8°$. This contrasts with their hypothetical $Pmn2_1$ counterpart Li$_4$SnS$_4^{iii}$ (Figure S7e), which only exhibits one reflection. Other regions marked gray exhibit similar behavior. This difference in diffraction patterns is likely attributed to the distinct Li site arrangements between the two phases.

Our DFT optimizations (using the r^{2}SCAN functional) revealed that the $Pnma$ phase (Li$_4$SnS$_4^i$ and Li$_4$SnS$_4^{ii}$) is the ground state structure of Li$_4$SnS$_4$, which is 8.12 meV/atom more stable than the theoretical $Pmn2_1$ Li$_4$SnS$_4^{iii}$ phase. This finding aligns with the local-density approximation study by Al-Qawasmeh et al.,[68] which also identified the $Pnma$ Li$_4$SnS$_4^{ii}$ (denoted as Li$_4$SnS$_4^0$ in their work) as the ground state. As the structural variations of Li$_4$SnS$_4$ have been addressed, we will omit superscripts in the rest of the paper.

Crystal Structure of Li$_4$Si$_{1-x}$Sn$_x$S$_4$ ($0 \leq x \leq 1$, $\Delta x = 0.1$). Based on the end member compounds o-Li$_4$SiS$_4$ and Li$_4$SnS$_4$, the full solid solution space of Li$_4$Si$_{1-x}$Sn$_x$S$_4$ ($0 \leq x \leq 1$, $\Delta x = 0.1$) was explored. Rietveld refinements of PXRD data were performed to elucidate the structure of the solid solution members. To ensure reproducibility for each stoichiometry, three samples were synthesized and subsequently characterized via Rietveld refinements. All samples appeared mostly phase pure, however, some still contained low amounts of Li$_2$S (max. 3.7 wt %, average 1.4 wt %) as an impurity phase. The Rietveld plots with the respective crystallographic data of all refinements are shown in the Supporting Information (Figures S8–S18 and Tables S9–S19).

Except for Li$_4$SnS$_4$ ($x = 1.0$), the o-Li$_4$SiS$_4$ structure, space group $Pmn2_1$, reported in this work was used as the starting

model for all Rietveld refinements of the PXRD data.[20,21,65,67] With increasing nominal tin content a linear, Vegard-type increase in unit cell volume and lattice parameters was observed (Figure 5a,b). Li$_4$SnS$_4$ differs slightly from the linear
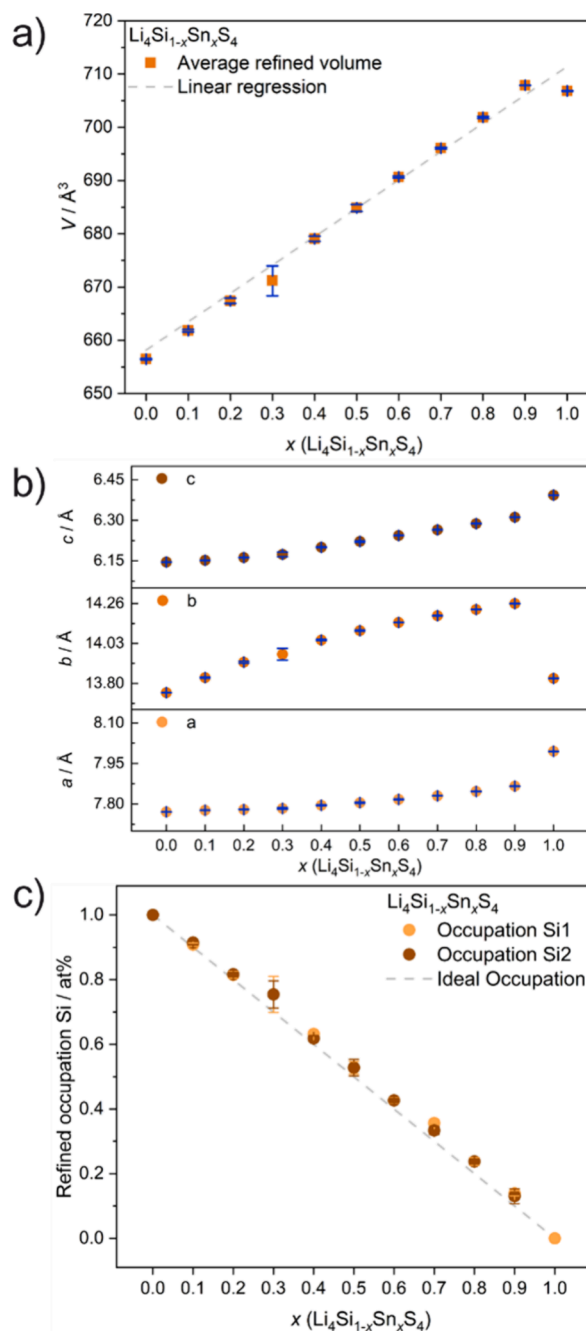

Figure 5. (a) Average refined volume and (b) average refined lattice parameters from PXRD plotted against the nominal substitution factor x in the Li$_4$Si$_{1-x}$Sn$_x$S$_4$ solid solution. For better comparison, the lattice parameters of Li$_4$SnS$_4$ are shown in the nonstandard setting $Pnmb$ ($a \leftrightarrow b$).[59] The dashed line in panel (a) represents a linear regression highlighting the Vegard behavior of the Li$_4$Si$_{1-x}$Sn$_x$S$_4$ solid solution.[69,70] (c) Average occupations of the Si1 and Si2 positions plotted against the substitution factor x in the Li$_4$Si$_{1-x}$Sn$_x$S$_4$ solid solution. The dashed line represents the ideal occupation. Data points shown in all graphs are the averages obtained from the refinements of three different samples. For clarity reasons in all graphs, only the standard deviation in the form of error bars is shown.
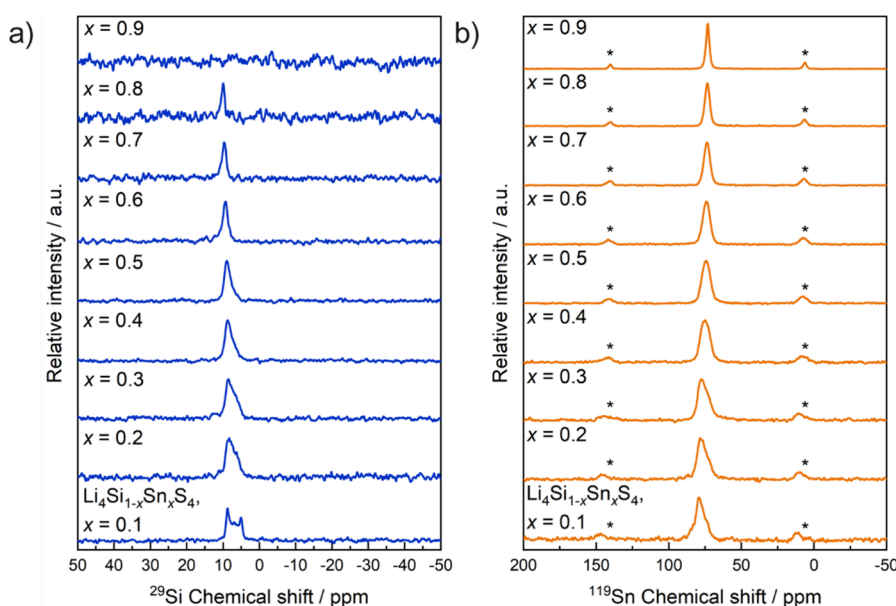
Figure 6. (a) ^{29}Si MAS NMR and (b) ^{119}Sn MAS NMR spectra of the $Li_4Si_{1-x}Sn_xS_4$ solid solution series ($0.1 \leq x \leq 0.9$) spun at 10 kHz. Spinning side bands are marked with asterisks.

Vegard trend, as its triplicate-derived average volume is slightly lower than the sample $x = 0.9$ (706.83(3) and 707.89(3) Å³, respectively), which can be explained with Li_4SnS_4 crystallizing in the disordered phase rather than in the ordered polymorph.[20,21,65,67] A similar trend appears when refining a mixed occupation with tin on the Si1 and Si2 positions (Figure 5c). The occupation of both positions was refined independently from each other, yet the refinements yielded very similar occupations for both Si positions, which also follow a linear Vegard-type trend and agree well with the weighed-in, nominal elemental composition. In general, the linear trends visible in Figure 5 show nearly full solubility of the two end members o-Li_4SiS_4 and Li_4SnS_4.[69,70] Representative SEM micrographs for all solid solution compositions are shown in Figures S19−S29, which confirm the polycrystalline and homogeneous nature of all samples. EDS spectra (Tables S20−S30) confirm the chemical composition for all samples.

Within the $Li_4Si_{1-x}Sn_xS_4$ solid solution, we focused on the $x = 0.5$ composition ($Li_4Si_{0.5}Sn_{0.5}S_4$) and performed first-principle DFT calculations to validate our findings. The lowest-energy ordered configuration of $Li_4Si_{0.5}Sn_{0.5}S_4$ was identified by exploring 4 distinct orderings within the conventional unit cell and 20 orderings within a $1 \times 1 \times 2$ supercell model. This stable configuration exhibits the same $Pmn2_1$ space group symmetry as the experimentally observed structure. A formation energy of −0.3 meV/atom with respect to two parent materials $Pmn2_1$ o-Li_4SiS_4 and $Pnma$ Li_4SnS_4 end members suggests that the $Li_4Si_{0.5}Sn_{0.5}S_4$ phase is thermodynamically stable and that its synthesis may be feasible.

Figure S30 compares the experimental and predicted model structures (from DFT) of the ground state structures of $Li_4Si_{0.5}Sn_{0.5}S_4$, whereas Table S31 provides a summary of the lattice constants and fractional atomic coordinates of these models. Although the calculated structure closely mirrors the experimental one in terms of Li and S ion positions, it exhibits a preferential ordering of the Si and Sn sites, with Si1 fully occupying the 2a site at (0, 0.664, 0.358) and Sn1 exclusively occupying another 2a site at (1/2, 0.840, 0.640). As illustrated in Figure S30b, the computed ordered arrangement results in

the alternating apex orientations of the SiS_4 and SnS_4 tetrahedra. A preferential Sn substitution of one Si site over the other, e.g. similarly to the Sn and P site ordering found in $Li_{10}SnP_2S_{12}$,[71,72] may be plausible due to the large radii difference between Si^{4+} and Sn^{4+}.[73] However, this result appears in contrast with our experimental results. During the Rietveld refinements the occupancies of both Si positions with Sn were freely refined, resulting in very similar occupancies for both sites (Figure 5c).

Figure 6a shows the ^{29}Si and ^{119}Sn solid-state MAS NMR spectra of the solid solution members $0.1 \leq x \leq 0.9$. The signals in the ^{29}Si NMR are in the chemical shift range of 4−11 ppm, which are in good agreement with the chemical shift range of SiS_4 tetrahedra groups.[51,52] Compared with the sharp signals in o-Li_4SiS_4 (Figure 2a) starting from the compositions with Sn content ($x \geq 0.1$) the peaks broaden significantly. Even small amounts of tin when incorporated seem to strongly influence the local structure surrounding both Si sites. We hypothesize that the broadening is probably due to the size difference of Si^{4+} and Sn^{4+} cations triggering site disorder.[73] With increasing tin content starting from composition $x \geq 0.3$ the peaks seem to merge into one peak, yet the peak shape remains asymmetric, still suggesting the presence of two signals. For $x = 0.9$, even after 45 h of acquisition time, no ^{29}Si NMR signal was detected. Taking into account the low silicon content in the $x = 0.9$ sample and the relatively low natural abundance of ^{29}Si, the silicon content is probably too low to yield a sufficient signal for that composition.[74] The correct composition was confirmed using EDS (see Table S29).

All ^{119}Sn NMR spectra (Figure 6b) show signals between 50 and 100 ppm, as typically found for SnS_4 tetrahedra. Due to the broad chemical shift range of ^{119}Sn and with the absence of any other signals the presence of Sn(+II) and SnS_6 octahedra can be excluded.[75] Similarly, the ^{119}Sn NMR spectrum for composition $x = 0.1$ shows one broad, asymmetric signal, also indicating the presence of two peaks as observed in the o-Li_4SiS_4 structure, and our Rietveld refinements (Figure 5c). With increasing tin content up to $x = 0.9$ the peaks narrow and become more symmetric, an indication that the local
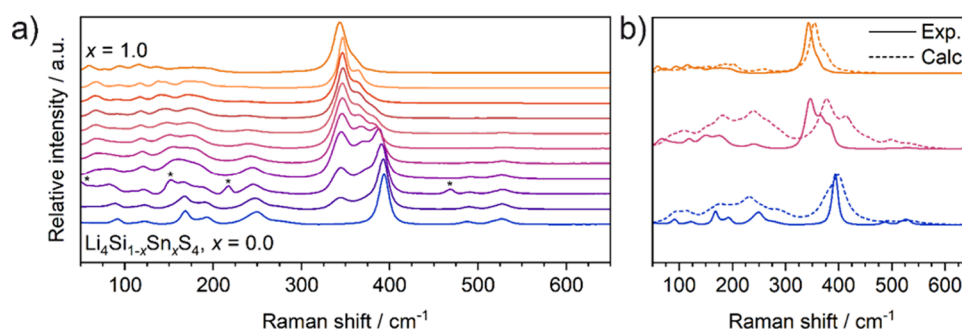
Figure 7. (a) Raman spectra (excitation 785 nm) of the full $Li_4Si_{1-x}Sn_xS_4$ solid solution series. Asterisks in the spectrum of $x = 0.2$ denote vibrations assigned to residual sulfur (see Figure S31).[76,77] (b) Comparison of experimental (solid lines) and calculated (dashed lines) Raman spectra for compositions $x = 0.0$, 0.5, and 1.0. Calculated spectra were generated by convoluting Raman-active modes from Tables S3, S32, and S33 with a Lorentzian line shape (fwhm = 15 cm^{-1}) assuming a 785 nm wavelength as used in the experimental measurements.

environments near the Sn atoms appear more similar. Since Li_4SnS_4 ($x = 1.0$) crystallizes in a different structure than all other solid solution members and the ^{119}Sn NMR spectrum of Li_4SnS_4 having been already reported by Kaib et al., its spectrum is not discussed here.[20,21,65,67]

Figure 7a shows the Raman spectra of all solid solution members, while the calculated spectra for select compositions ($x = 0.0$, 0.5, and 1.0) are shown in Figure 7b. The most intense bands are found in the region between 320 and 420 cm^{-1}. Starting at $x = 0.1$, in addition to the main SiS_4 symmetric stretching band at 393 cm^{-1}, another band surfaces at 347 cm^{-1}, which can be assigned to the symmetric stretching vibration of the SnS_4 tetrahedron.[26,27,78] In addition to the main SnS_4 band a shoulder at ~362 cm^{-1} starts to emerge, which is present in all spectra of tin-containing compounds. In general, the calculated Raman spectrum for the $x = 0.5$ composition (Figure 7b and Table S32) closely matches the experimental observations, particularly in the 300–450 cm^{-1} range where shoulder peaks are present. Furthermore, the two main calculated peaks at 377 cm^{-1} and 415 cm^{-1} can be associated to asymmetric stretching (A_1 mode) of the distinct SiS_4 and SnS_4 tetrahedral units. In literature Raman spectra of Li_4SnS_4 the shoulder is sometimes present[78,79] or absent.[26,27,29] The absence of the shoulder may be explained by overlap with the main SnS_4 symmetric stretching band caused by signal broadening due to different degrees of crystallinity. Yet, even when present, the shoulder was not assigned properly.[78,79] Nonetheless, when comparing the Li_4SnS_4 Raman spectrum with the one of its heavier homologue, K_4SnS_4, it is reasonable to assume the shoulder at 362 cm^{-1} could be the result of an asymmetric vibration of the SnS_4 tetrahedron.[80] In addition, our calculated Raman spectrum of Li_4SnS_4 in Figure 7b and Table S33 shows a shoulder peak at 376 cm^{-1}, which we assigned to an asymmetric vibration of the SnS_4 tetrahedron.

Beside the most intense SiS_4 and SnS_4 bands, additional signals in the range of 50–300 cm^{-1} and 450–550 cm^{-1} are visible. Starting from composition $x = 0.0$, with increasing tin content some signals in those regions lose intensity, while others only shift toward lower inverse wavenumbers. Since the signals that loose intensity are also present in the o-Li_4SiS_4 spectrum, it can be assumed that those also belong to some vibrational modes of the SiS_4 tetrahedron. With decreasing SiS_4 concentration, it is expected for these vibrational SiS_4 modes to lose intensity. Bands shifting toward lower wavenumbers with increasing tin content may be due to lattice vibrations. Since tin has a significantly heavier atomic mass than silicon (Si: 28.085 u; Sn: 118.71 u),[81] lattice vibrations are expected to

redshift toward lower wavenumbers.[82] This trend is corroborated by our simulation results, as depicted in Figure 7b. In summary, the Raman spectra of the $Li_4Si_{1-x}Sn_xS_4$ solid solution confirm the presence of SiS_4 and SnS_4 tetrahedra and show expected behavior in accordance with the nominal tin content.

Transport Properties. To elucidate the Li-ion transport properties of the $Li_4Si_{1-x}Sn_xS_4$ solid solution series, EIS measurements were carried out. All spectra were fitted using equivalent circuits composed of a series of resistors and constant phase elements (CPEs) in parallel to model semicircles. Polarization at the electrode−sample interface was modeled with an additional CPE in series. To assign bulk and grain boundary contributions the Brug capacity C_{Brug} of all CPEs was used.[83,84] Since it was not possible to resolve bulk and grain boundary contributions in all spectra only the total Li-ion conductivities are reported here. For the calculation of the total ionic conductivity only semicircles with a C_{Brug} of 10^{-10} F or lower were considered, since these are attributable to bulk and grain boundary processes. In some spectra semicircles attributable to sample−electrode processes ($C_{Brug} \geq 10^{-7}$ F) were visible. These semicircles were fitted, but not included in the calculation of the ionic conductivity.[85]

Figure 8 gives an overview of the ionic conductivities and activation energies of all solid solution members. Nyquist plots and Arrhenius graphs for determination of the activation energies for all samples are shown in the Supporting Information (Figures S32−S42). All members of the $Li_4Si_{1-x}Sn_xS_4$ solid solution series show average ionic conductivities in the range of ~10^{-6} S cm^{-1} at 25 °C. The end members o-Li_4SiS_4 and Li_4SnS_4 have average conductivities of 1.5×10^{-6} S cm^{-1} and 3.7×10^{-6} S cm^{-1} at the same temperature, which aligns with reports from the literature.[24,65,67] Although, in general no clear trend between composition x and the ionic conductivity and activation energy is visible, both the highest average ionic conductivity and lowest activation energy are found for $x = 0.5$. $Li_4Si_{0.5}Sn_{0.5}S_4$ shows an average ionic conductivity of 8.4×10^{-6} S cm^{-1} (maximum 1.4×10^{-5} S cm^{-1}) at 25 °C, which is more than twice compared to the conductivities of the end members o-Li_4SiS_4 and Li_4SnS_4, with the best sample reaching 1.4×10^{-5} S cm^{-1} at 25 °C. The average activation energy of $Li_4Si_{0.5}Sn_{0.5}S_4$ is 0.37 eV, which is significantly lower than the average activation energy for o-Li_4SiS_4 (0.43 eV) and comparable to that of Li_4SnS_4 (0.38 eV).

One way to gain insight into the lithium ion transport mechanism and to further classify SEs is to look at the relationship of the Arrhenius pre-exponential factor σ_0 and the
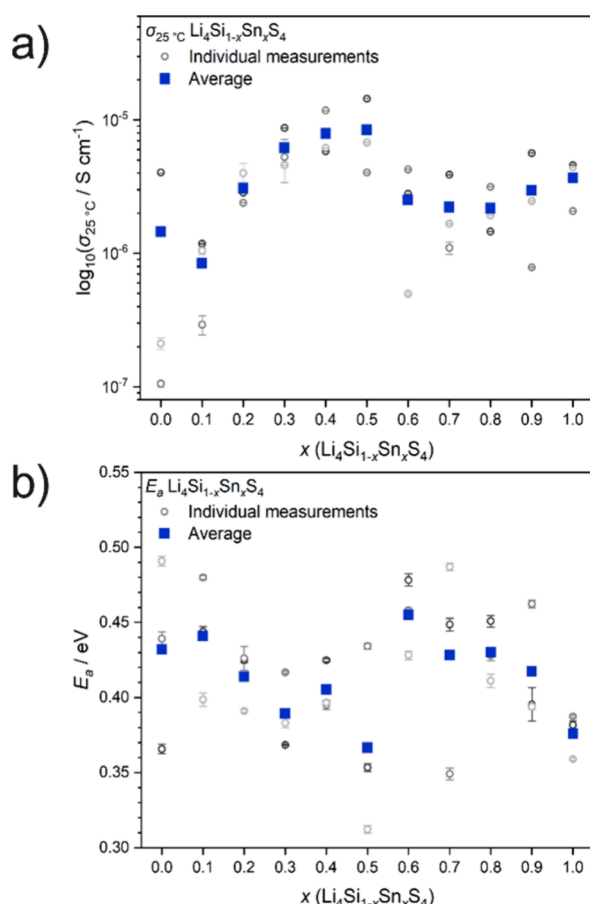
Figure 8. (a) Total Li-ion conductivities σ at 25 °C and (b) derived activation energies E_a of the complete $Li_4Si_{1-x}Sn_xS_4$ solid solution series. The results from individual measurements are represented by empty circles, while the respective averages of all three measurements for each stoichiometry are depicted as filled squares.

activation energy E_a using the Meyer–Neldel rule.[86−88] The rule implies that for a series of similar compounds (e.g., a solid solution series) there is a linear relationship between σ_0 and E_a, which can be expressed as $\ln(\sigma_0) = \alpha E_a + \beta$, with α and β being constants.[89] The so-called Meyer–Neldel energy Δ_0 is defined as α^{-1} and can be obtained by plotting $\ln(\sigma_0)$ against E_a. By combining the modified Arrhenius equation and Meyer–Neldel relationship the equation $\sigma = e^{(\frac{1}{\Delta_0} - \frac{1}{k_B T})E_a + \beta} T^{-1}$ is obtained. This implies that σ and E_a are dependent on the relative magnitude of Δ_0 to the thermal energy $k_B T$ (~26 meV at 25 °C).[87,90,91] Comparing Δ_0 to $k_B T$ then reveals whether E_a and the ionic conductivity σ are indirectly proportional ($\Delta_0 > k_B T$, Type 1), directly proportional ($\Delta_0 < k_B T$, Type 2), or independent ($\Delta_0 \approx k_B T$, Type 3) from each other. Analyzing this relationship for the $Li_4Si_{1-x}Sn_xS_4$ solid solution series (see Figure S43) a value of 59 meV for Δ_0 is obtained, which is significantly larger than $k_B T$, and hence classifying the series as Type 1 SEs, implying that a lower E_a will lead to higher conductivities σ (see Figure S44).[87,90]

This, however, does not explain the absence of a linear trend in σ and E_a, across the solid solution series, with the exact cause of this being unclear. While for some samples the Arrhenius prefactor σ_0 has a large variation (see Figure S45), no direct correlation to the spread in σ and E_a is visible. Generally, the ionic conductivity can be influenced by multiple, often convoluted parameters. Structural parameters influencing

the conductivity include, among others, changes in cation and anion sublattice, diffusion path volume and jumping distances, and lattice flexibility.[92] Here, the lithium sublattice should not change significantly, since the substitution of Si^{4+} with Sn^{4+} is isovalent, and hence the charge carrier concentration remains the same, a result which was also found for the isovalent substitution of Sn into Li_4GeS_4, the heavier homologue of o-Li_4SiS_4.[67] Microstructural effects, such as different grain size distributions and grain boundaries and varying pellet densities might also influence the ionic conductivity.[93] Lastly, entropic effects may also play a role. This could explain why the maximum for σ is found at $x = 0.5$, since here the configurational entropy caused by 1:1 mixed occupation of the Si sites with and Sn is largest.[94] Summarizing, we believe that the nonlinear trend observed for σ and E_a cannot be pinpointed to a single effect and is most likely caused by several effects acting together.

■ CONCLUSIONS

Using SXRD data we showed that o-Li_4SiS_4 crystallizes in a different symmetry than previously known. Due to additional reflections observed in the $0kl$ precession image, which are not aligned with the zonal reflection condition for a glide planes, the structure of o-Li_4SiS_4 was solved in $Pmn2_1$ rather than $Pnma$. First-principles calculations, based on DFT, also show that the $Pmn2_1$ phase is the preferred phase at RT. Ultimately, for the case of o-Li_4SiS_4, we highlighted the importance of using local methods, such as MAS NMR and Raman spectroscopy together with DFT optimization to identify subtle structural details of crystal structures.

Furthermore, we showed that it is possible to fully substitute silicon in o-Li_4SiS_4 with tin. The solid solution series $Li_4Si_{1-x}Sn_xS_4$ shows a nearly linear Vegard behavior up to $x = 0.9$, while Li_4SnS_4 crystallizes in a different structure type and slightly deviates from the Vegard trend. The ^{29}Si and ^{119}Sn MAS NMR spectra showed signals in accordance with SiS_4 and SnS_4 tetrahedra and clear shifts regarding the silicon−tin ratio were observable. Similarly, the experimental and calculated Raman spectra allowed identification of the stretching bands of the SiS_4 and SnS_4 tetrahedra, which are consistent with the structural analyses. Lastly, we were successful in increasing the ionic conductivity of o-Li_4SiS_4 by tin substitution. $Li_4Si_{0.5}Sn_{0.5}S_4$ showed the highest average ionic conductivity of 8.4×10^{-6} S cm^{-1} (maximum 1.4×10^{-5} S cm^{-1}) at 25 °C, which is more than twice what was obtained for o-Li_4SiS_4 and Li_4SnS_4. Hence, our work serves as a starting and reference point for the development of new highly conducting, earth-abundant and air-stable SEs.

■ ASSOCIATED CONTENT

Data Availability Statement

The data supporting this study have been included in the supporting information and are available from the authors upon reasonable request.

Ⓢ Supporting Information

The Supporting Information is available free of charge at https://pubs.acs.org/doi/10.1021/acs.chemmater.5c00358.

Additional crystallographic data on o-Li_4SiS_4, Raman simulations of o-Li_4SiS_4, group−subgroup relationships of o-Li_4SiS_4, additional data on DFT optimizations of the o-Li_4SiS_4 and Li_4SnS_4 structures, Rietveld refinement plots and data, SEM micrographs, EDS data, additional

data on DFT optimizations of the $Li_4Si_{0.5}Sn_{0.5}S_4$ structure, Raman spectrum of $Li_4Si_{1-x}Sn_xS_4$ (x = 0.2), Raman simulations of $Li_4Si_{1-x}Sn_xS_4$ (x = 0.5 and 1.0), additional data on EIS measurements (PDF)

Accession Codes

Deposition Number 2415854 contains the supplementary crystallographic data for this paper. These data can be obtained free of charge via the joint Cambridge Crystallographic Data Centre (CCDC) and Fachinformationszentrum Karlsruhe Access Structures service.

■ AUTHOR INFORMATION

Corresponding Authors

Pieremanuele Canepa − *Department of Materials Science and Engineering, National University of Singapore, Singapore 117575, Singapore; Department of Electrical and Computer Engineering, University of Houston, Houston, Texas 77204, United States; Texas Center for Superconductivity, University of Houston, Houston, Texas 77204, United States;* ● orcid.org/0000-0002-5168-9253; Email: pcanepa@uh.edu

Bettina V. Lotsch − *Department of Nanochemistry, Max Planck Institute for Solid State Research, Stuttgart 70569, Germany; Department of Chemistry, Ludwig Maximilian University Munich, Munich 81377, Germany; E-Conversion, Garching 85748, Germany;* ● orcid.org/0000-0002-3094-303X; Email: b.lotsch@fkf.mpg.de

Authors

Lucas G. Balzat − *Department of Nanochemistry, Max Planck Institute for Solid State Research, Stuttgart 70569, Germany; Department of Chemistry, Ludwig Maximilian University Munich, Munich 81377, Germany;* ● orcid.org/0009-0008-0409-2383

Yan Li − *Department of Materials Science and Engineering, National University of Singapore, Singapore 117575, Singapore*

Sascha Dums − *Department of Nanochemistry, Max Planck Institute for Solid State Research, Stuttgart 70569, Germany; Department of Chemistry, Ludwig Maximilian University Munich, Munich 81377, Germany*

Igor Moudrakovski − *Department of Nanochemistry, Max Planck Institute for Solid State Research, Stuttgart 70569, Germany;* ● orcid.org/0000-0002-8919-4766

Kristina Gjorgjevikj − *Department of Nanochemistry, Max Planck Institute for Solid State Research, Stuttgart 70569, Germany;* ● orcid.org/0000-0002-1860-7025

Armin Schulz − *Department of Nanochemistry, Max Planck Institute for Solid State Research, Stuttgart 70569, Germany*

Yuheng Li − *Department of Materials Science and Engineering, National University of Singapore, Singapore 117575, Singapore;* ● orcid.org/0000-0002-1865-1122

Simon Krause − *Department of Nanochemistry, Max Planck Institute for Solid State Research, Stuttgart 70569, Germany;* ● orcid.org/0000-0001-9504-8514

Complete contact information is available at:
https://pubs.acs.org/10.1021/acs.chemmater.5c00358

Author Contributions

L.G.B. performed the material synthesis, measured the PXRD and EIS, and analyzed the PXRD, SEM, EDS, NMR, Raman, and EIS data. Y.L. performed the theoretical calculations with discussions from Y.H.L. S.D. solved the o-Li_4SiS_4 structure from the SXRD data. I.M. measured the solid-state NMR spectra. A.S., K.G., and S.K. recorded the Raman spectra. This manuscript was written through contributions from L.G.B. (crystallography, SEM, EDS, NMR, Raman, and EIS) and Y.L. (theoretical calculations). All authors have read, commented on, and given approval to the final version of the manuscript.

■ REFERENCES

(1) Janek, J.; Zeier, W. G. A solid future for battery development. *Nat. Energy* **2016**, *1* (9), 16141.

(2) Janek, J.; Zeier, W. G. Challenges in speeding up solid-state battery development. *Nat. Energy* **2023**, *8* (3), 230−240.

(3) Lau, J.; DeBlock, R. H.; Butts, D. M.; Ashby, D. S.; Choi, C. S.; Dunn, B. S. Sulfide Solid Electrolytes for Lithium Battery Applications. *Adv. Energy Mater.* **2018**, *8* (27), 1800933.

(4) Kamaya, N.; Homma, K.; Yamakawa, Y.; Hirayama, M.; Kanno, R.; Yonemura, M.; Kamiyama, T.; Kato, Y.; Hama, S.; Kawamoto, K.; et al. A lithium superionic conductor. *Nat. Mater.* **2011**, *10* (9), 682−686.

(5) Adeli, P.; Bazak, J. D.; Park, K. H.; Kochetkov, I.; Huq, A.; Goward, G. R.; Nazar, L. F. Boosting Solid-State Diffusivity and Conductivity in Lithium Superionic Argyrodites by Halide Substitution. *Angew. Chem., Int. Ed.* **2019**, *58* (26), 8681−8686.

(6) Kato, Y.; Hori, S.; Saito, T.; Suzuki, K.; Hirayama, M.; Mitsui, A.; Yonemura, M.; Iba, H.; Kanno, R. High-power all-solid-state batteries using sulfide superionic conductors. *Nat. Energy* **2016**, *1* (4), 16030.

(7) Li, Y.; Song, S.; Kim, H.; Nomoto, K.; Kim, H.; Sun, X.; Hori, S.; Suzuki, K.; Matsui, N.; Hirayama, M.; et al. A lithium superionic conductor for millimeter-thick battery electrode. *Science* **2023**, *381* (6653), 50−53.

(8) Xu, K. Nonaqueous Liquid Electrolytes for Lithium-Based Rechargeable Batteries. *Chem. Rev.* **2004**, *104* (10), 4303−4418.

(9) Yaroshevsky, A. A. Abundances of chemical elements in the Earth's crust. *Geochem. Int.* **2006**, *44* (1), 48−55.

(10) Hong, H. Y. P. Crystal-Structure and Ionic-Conductivity of Li14Zn(GeO4)4 and Other New Li+ Superionic Conductors. *Mater. Res. Bull.* **1978**, *13* (2), 117−124.

(11) Tao, B.; Ren, C.; Li, H.; Liu, B.; Jia, X.; Dong, X.; Zhang, S.; Chang, H. Thio-/LISICON and LGPS-Type Solid Electrolytes for All-Solid-State Lithium-Ion Batteries. *Adv. Funct. Mater.* **2022**, *32* (34), 2203551.

(12) Kanno, R.; Hata, T.; Kawamoto, Y.; Irie, M. Synthesis of a new lithium ionic conductor, thio-LISICON-lithium germanium sulfide system. *Solid State Ionics* **2000**, *130* (1−2), 97−104.

(13) Pearson, R. G. Hard and Soft Acids and Bases. *J. Am. Chem. Soc.* **1963**, *85* (22), 3533−3539.

(14) Baur, W. H.; Ohta, T. The Crystal-Structure of Li3.75si0.75-p0.25o4 and Ionic-Conductivity in Tetrahedral Structures. *J. Solid State Chem.* **1982**, *44* (1), 50−59.

(15) Wang, B.; Chakoumakos, B. C.; Sales, B. C.; Kwak, B. S.; Bates, J. B. Synthesis, Crystal Structure, and Ionic Conductivity of a Polycrystalline Lithium Phosphorus Oxynitride with the γ-Li3PO4 Structure. *J. Solid State Chem.* **1995**, *115* (2), 313−323.

(16) Ahn, B. T.; Huggins, R. A. Synthesis and Lithium Conductivities of Li2SiS3 and Li4SiS4. *Mater. Res. Bull.* **1989**, *24* (7), 889−897.

(17) Murayama, M.; Kanno, R.; Irie, M.; Ito, S.; Hata, T.; Sonoyama, N.; Kawamoto, Y. Synthesis of New Lithium Ionic Conductor Thio-LISICON—Lithium Silicon Sulfides System. *J. Solid State Chem.* **2002**, *168* (1), 140−148.

(18) Kanno, R.; Murayama, M. Lithium Ionic Conductor Thio-LISICON: The Li2S GeS2 P2S5 System. *J. Electrochem. Soc.* **2001**, *148* (7), A742.

(19) Murayama, M.; Kanno, R.; Kawamoto, Y.; Kamiyama, T. Structure of the thio-LISICON, Li4GeS4. *Solid State Ionics* **2002**, *154*, 789−794.

(20) Kaib, T.; Haddadpour, S.; Kapitein, M.; Bron, P.; Schröder, C.; Eckert, H.; Roling, B.; Dehnen, S. New Lithium Chalcogenidotetrelates, LiChT: Synthesis and Characterization of the Li+-Conducting Tetralithium ortho-Sulfidostannate Li4SnS4. *Chem. Mater.* **2012**, *24* (11), 2211−2219.

(21) MacNeil, J. H.; Massi, D. M.; Zhang, J. H.; Rosmus, K. A.; Brunetta, C. D.; Gentile, T. A.; Aitken, J. A. Synthesis, structure, physicochemical characterization and electronic structure of thio-lithium super ionic conductors, Li4GeS4 and Li4SnS4. *J. Alloys Compd.* **2014**, *586*, 736−744.

(22) Homma, K.; Yonemura, M.; Nagao, M.; Hirayama, M.; Kanno, R. Crystal Structure of High-Temperature Phase of Lithium Ionic Conductor, Li3PS4. *J. Phys. Soc. Jpn.* **2010**, *79* (Suppl.A), 90−93.

(23) Homma, K.; Yonemura, M.; Kobayashi, T.; Nagao, M.; Hirayama, M.; Kanno, R. Crystal structure and phase transitions of the lithium ionic conductor Li3PS4. *Solid State Ionics* **2011**, *182* (1), 53−58.

(24) Roh, J.; Kim, H.; Lee, H.; Bu, H.; Manjón-Sanz, A.; Kim, H.; Hong, S.-T. Unraveling Polymorphic Crystal Structures of Li4SiS4 for All-Solid-State Batteries: Enhanced Ionic Conductivity via Aliovalent Sb Substitution. *Chem. Mater.* **2024**, *36*, 6973.

(25) Matsuda, R.; Kokubo, T.; Phuc, N. H. H.; Muto, H.; Matsuda, A. Preparation of ambient air-stable electrolyte Li4SnS4 by aqueous ion-exchange process. *Solid State Ionics* **2020**, *345*, No. 115190.

(26) Kimura, T.; Nakano, T.; Sakuda, A.; Tatsumisago, M.; Hayashi, A. Hydration and Dehydration Behavior of Li4SnS4 for Applications as a Moisture-Resistant All-Solid-State Battery Electrolyte. *J. Phys. Chem. C* **2023**, *127* (3), 1303−1309.

(27) Morino, Y.; Otoyama, M.; Okumura, T.; Kuratani, K.; Shibata, N.; Ito, D.; Sano, H. Influence of Traces of Moisture on a Sulfide Solid Electrolyte Li4SnS4. *Electrochem.* **2024**, *92* (4), 047002−047002.

(28) Morino, Y.; Otoyama, M.; Okumura, T.; Kuratani, K.; Takemoto, S.; Ito, D.; Sano, H. Elucidating the Reductive

(29) Morino, Y.; Otoyama, M.; Okumura, T.; Kuratani, K.; Shibata, N.; Ito, D.; Sano, H. Concerted Influence of H2O and CO2: Moisture Exposure of Sulfide Solid Electrolyte Li4SnS4. *ACS Omega* **2024**, *9* (37), 38523.

(30) Krause, L.; Herbst-Irmer, R.; Sheldrick, G. M.; Stalke, D. Comparison of silver and molybdenum microfocus X-ray sources for single-crystal structure determination. *J. Appl. Crystallogr.* **2015**, *48* (Pt 1), 3−10.

(31) Sheldrick, G. M. A short history of SHELX. *Acta Crystallogr. Sect. A: Found. Crystallogr.* **2008**, *64* (Pt 1), 112−122.

(32) Momma, K.; Izumi, F. VESTA 3 for three-dimensional visualization of crystal, volumetric and morphology data. *J. Appl. Crystallogr.* **2011**, *44* (6), 1272−1276.

(33) Coelho, A. A. TOPAS and TOPAS-Academic: an optimization program integrating computer algebra and crystallographic objects written in C++. *J. Appl. Crystallogr.* **2018**, *51* (1), 210−218.

(34) Bielecki, A.; Burum, D. P. Temperature Dependence of 207 Pb MAS Spectra of Solid Lead Nitrate. An Accurate, Sensitive Thermometer for Variable-Temperature MAS. *J. Magn. Reson., Ser. A* **1995**, *116* (2), 215−220.

(35) Nuernberg, R. B. Numerical comparison of usual Arrhenius-type equations for modeling ionic transport in solids. *Ionics* **2020**, *26* (5), 2405−2412.

(36) Ohno, S.; Bernges, T.; Buchheim, J.; Duchardt, M.; Hatz, A.-K.; Kraft, M. A.; Kwak, H.; Santhosha, A. L.; Liu, Z.; Minafra, N.; et al. How Certain Are the Reported Ionic Conductivities of Thiophosphate-Based Solid Electrolytes? An Interlaboratory Study. *ACS Energy Lett.* **2020**, *5* (3), 910−915.

(37) Kohn, W.; Sham, L. J. Self-Consistent Equations Including Exchange and Correlation Effects. *Phys. Rev.* **1965**, *140* (4A), A1133−A1138.

(38) Kresse, G.; Furthmüller, J. Efficient iterative schemes for ab initio total-energy calculations using a plane-wave basis set. *Phys. Rev. B* **1996**, *54* (16), 11169−11186.

(39) Kresse, G.; Joubert, D. From ultrasoft pseudopotentials to the projector augmented-wave method. *Phys. Rev. B* **1999**, *59* (3), 1758−1775.

(40) Furness, J. W.; Kaplan, A. D.; Ning, J.; Perdew, J. P.; Sun, J. Accurate and Numerically Efficient r2SCAN Meta-Generalized Gradient Approximation. *J. Phys. Chem. Lett.* **2020**, *11* (19), 8208−8215.

(41) Sun, J.; Ruzsinszky, A.; Perdew, J. P. Strongly Constrained and Appropriately Normed Semilocal Density Functional. *Phys. Rev. Lett.* **2015**, *115* (3), No. 036402.

(42) Kingsbury, R.; Gupta, A. S.; Bartel, C. J.; Munro, J. M.; Dwaraknath, S.; Horton, M.; Persson, K. A. Performance comparison of r2SCAN and SCAN metaGGA density functionals for solid materials via an automated, high-throughput computational workflow. *Phys. Rev. Mater.* **2022**, *6* (1), No. 013801.

(43) Blöchl, P. E. Projector augmented-wave method. *Phys. Rev. B* **1994**, *50* (24), 17953−17979.

(44) Erba, A.; Desmarais, J. K.; Casassa, S.; Civalleri, B.; Donà, L.; Bush, I. J.; Searle, B.; Maschio, L.; Edith-Daga, L.; Cossard, A.; et al. CRYSTAL23: A Program for Computational Solid State Physics and Chemistry. *J. Chem. Theory Comput.* **2023**, *19* (20), 6891−6932.

(45) Adamo, C.; Barone, V. Toward reliable density functional methods without adjustable parameters: The PBE0 model. *J. Chem. Phys.* **1999**, *110* (13), 6158−6170.

(46) Li, Y.; Lee, D. K. J.; Cai, P.; Zhang, Z.; Gorai, P.; Canepa, P. A database of computed Raman spectra of inorganic compounds with accurate hybrid functionals. *Sci. Data* **2024**, *11* (1), 105.

(47) Vilela Oliveira, D.; Laun, J.; Peintinger, M. F.; Bredow, T. BSSE-correction scheme for consistent gaussian basis sets of double- and triple-zeta valence with polarization quality for solid-state calculations. *J. Comput. Chem.* **2019**, *40* (27), 2364−2376.

(48) Dolg, M. Relativistic Effective Core Potentials. In *Handbook of Relativistic Quantum Chemistry*; Liu, W., Ed.; Springer: Berlin Heidelberg, 2017; pp 449−478.

(49) Togo, A. First-principles Phonon Calculations with Phonopy and Phono3py. *J. Phys. Soc. Jpn.* **2023**, *92* (1), No. 012001.

(50) Krebs, B.; Mandt, J. Zur Kenntnis des Argyrodit-Strukturtyps: Die Kristallstruktur von Ag8SiS6/The Argyrodite Structure Type: The Crystal Structure of Ag8SiS6. *Z. Naturforsch. B* **1977**, *32* (4), 373−379.

(51) Watson, D. E.; Martin, S. W. Short range order characterization of the Na2S+SiS2 glass system using Raman, infrared and 29Si magic angle spinning nuclear magnetic resonance spectroscopies. *J. Non-Cryst. Solids* **2017**, *471*, 39−50.

(52) Harm, S.; Hatz, A. K.; Moudrakovski, I.; Eger, R.; Kuhn, A.; Hoch, C.; Lotsch, B. V. Lesson Learned from NMR: Characterization and Ionic Conductivity of LGPS-like Li7SiPS8. *Chem. Mater.* **2019**, *31* (4), 1280−1288.

(53) Eckert, H.; Zhang, Z.; Kennedy, J. H. Glass formation in non-oxide chalcogenide systems. Structural elucidation of Li2-SiS2-LiI solid electrolytes by quantitative 29Si, 6Li and 7Li high resolution solid state NMR methods. *J. Non-Cryst. Solids* **1989**, *107* (2−3), 271−282.

(54) Hartenbach, I.; Gerlach, I.; Schleid, T. Mixed-Valent Europium in the Cubic Thiosilicate Li3Eu6[SiS4]4. *Z. Anorg. Allg. Chem.* **2019**, *645* (3), 149−152.

(55) Calaminus, R.; Harm, S.; Fabini, D. H.; Balzat, L. G.; Hatz, A.-K.; Duppel, V.; Moudrakovski, I.; Lotsch, B. V. Enhancing Ionic Conductivity by in Situ Formation of Li7SiPS8/Argyrodite Hybrid Solid Electrolytes. *Chem. Mater.* **2022**, *34* (17), 7666−7677.

(56) Kim, K. H.; Martin, S. W. Structures and Properties of Oxygen-Substituted Li10SiP2S12−xOx Solid-State Electrolytes. *Chem. Mater.* **2019**, *31* (11), 3984−3991.

(57) Kamitsos, E. I.; Yiannopoulos, Y. D.; Jain, H.; Huang, W. C. Far-infrared spectra of alkali germanate glasses and correlation with electrical conductivity. *Phys. Rev. B: Condens. Matter* **1996**, *54* (14), 9775−9783.

(58) Kamitsos, E. I.; Chryssikos, G. D.; Patsis, A. P.; Duffy, J. A. Metal ion sites in oxide glasses - Relation to glass basicity and ion transport. *J. Non-Cryst. Solids* **1996**, *196*, 249−254.

(59) Space group 62. In *International Tables for Crystallography Volume A: Space Group Symmetry*; 5th reprinted ed.; Hahn, T. Ed.; Springer, 2006; pp 298−299.

(60) Space group 31. In *International Tables for Crystallography Volume A: Space Group Symmetry*; 5th reprinted ed.; Hahn, T. Ed.; Springer, 2006; pp 230−231.

(61) Billiet, Y.; Aroyo, M. I.; Wondratschek, H. Maximal subgroups of space group 62. In *International Tables for Crystallography Volume A1: Symmetry Relations between Space Groups*; Wondratschek, H.; Müller, U. Eds.; Kluwer Academic Publishers, 2004; p 176.

(62) Müller, U. Wyckoff relations for space group 62. In *International Tables for Crystallography Volume A1: Symmetry Relations between Space Groups*; Wondratschek, H.; Müller, U. Eds.; Kluwer Academic Publishers, 2004; p 530.

(63) Müller, U. Kristallographische Gruppe-Untergruppe-Beziehungen und ihre Anwendung in der Kristallchemie. *Z. Anorg. Allg. Chem.* **2004**, *630* (11), 1519−1537.

(64) Block, T.; Seidel, S.; Pöttgen, R. Bärnighausen Trees − A group−subgroup reference database. *Z. Kristallogr. Cryst. Mater.* **2022**, *237* (6−7), 215−218.

(65) Kwak, H.; Park, K. H.; Han, D.; Nam, K. W.; Kim, H.; Jung, Y. S. Li+ conduction in air-stable Sb-Substituted Li4SnS4 for all-solid-state Li-Ion batteries. *J. Power Sources* **2020**, *446*, No. 227338.

(66) Li, Y.; Hood, Z. D.; Holzwarth, N. A. W. Computational and experimental (re)investigation of the structural and electrolyte properties of Li4P2S6, Na4P2S6, and Li2Na2P2S6. *Phys. Rev. Mater.* **2020**, *4* (4), No. 045406.

(67) Minafra, N.; Culver, S. P.; Li, C.; Senyshyn, A.; Zeier, W. G. Influence of the Lithium Substructure on the Diffusion Pathways and Transport Properties of the Thio-LISICON Li4Ge1-xSnxS4. *Chem. Mater.* **2019**, *31* (10), 3794−3802.

(68) Al-Qawasmeh, A.; Howard, J.; Holzwarth, N. A. W. Li4SnS4 and Li4SnSe4: Simulations of Their Structure and Electrolyte Properties. *J. Electrochem. Soc.* **2017**, *164* (1), A6386.

(69) Vegard, L. Die Konstitution der Mischkristalle und die Raumfüllung der Atome. *Z. Phys.* **1921**, *5* (1), 17−26.

(70) Denton, A. R.; Ashcroft, N. W. Vegard's law. *Phys. Rev. A: At. Mol. Opt. Phys.* **1991**, *43* (6), 3161−3164.

(71) Kuhn, A.; Gerbig, O.; Zhu, C.; Falkenberg, F.; Maier, J.; Lotsch, B. V. A new ultrafast superionic Li-conductor: ion dynamics in Li11Si2PS12 and comparison with other tetragonal LGPS-type electrolytes. *Phys. Chem. Chem. Phys.* **2014**, *16* (28), 14669−14674.

(72) Bron, P.; Johansson, S.; Zick, K.; Schmedt auf der Gunne, J.; Dehnen, S.; Roling, B. Li10SnP2S12: an affordable lithium superionic conductor. *J. Am. Chem. Soc.* **2013**, *135* (42), 15694−15697.

(73) Shannon, R. D. Revised Effective Ionic-Radii and Systematic Studies of Interatomic Distances in Halides and Chalcogenides. *Acta Crystallogr., Sect. A* **1976**, *32*, 751−767.

(74) Meija, J.; Coplen, T. B.; Berglund, M.; Brand, W. A.; Bièvre, P. D.; Gröning, M.; Holden, N. E.; Irrgeher, J.; Loss, R. D.; Walczyk, T.; et al. Isotopic compositions of the elements 2013 (IUPAC Technical Report). *Pure Appl. Chem.* **2016**, *88* (3), 293−306.

(75) Mundus, C.; Taillades, G.; Pradel, A.; Ribes, M. A 119Sn solid-state nuclear magnetic resonance study of crystalline tin sulphides. *Solid State Nucl. Magn. Reson.* **1996**, *7* (2), 141−146.

(76) Harvey, P. D.; Butler, I. S. Raman-Spectra of Orthorhombic Sulfur at 40 K. *J. Raman Spectrosc.* **1986**, *17* (4), 329−334.

(77) Trofimov, B. A.; Sinegovskaya, L. M.; Gusarova, N. K. Vibrations of the S−S bond in elemental sulfur and organic polysulfides: a structural guide. *J. Sulfur Chem.* **2009**, *30* (5), 518−554.

(78) Kanazawa, K.; Yubuchi, S.; Hotehama, C.; Otoyama, M.; Shimono, S.; Ishibashi, H.; Kubota, Y.; Sakuda, A.; Hayashi, A.; Tatsumisago, M. Mechanochemical Synthesis and Characterization of Metastable Hexagonal Li(4)SnS(4) Solid Electrolyte. *Inorg. Chem.* **2018**, *57* (16), 9925−9930.

(79) Choi, Y. E.; Park, K. H.; Kim, D. H.; Oh, D. Y.; Kwak, H. R.; Lee, Y. G.; Jung, Y. S. Coatable Li(4) SnS(4) Solid Electrolytes Prepared from Aqueous Solutions for All-Solid-State Lithium-Ion Batteries. *ChemSusChem* **2017**, *10* (12), 2605−2611.

(80) Protesescu, L.; Nachtegaal, M.; Voznyy, O.; Borovinskaya, O.; Rossini, A. J.; Emsley, L.; Copéret, C.; Günther, D.; Sargent, E. H.; Kovalenko, M. V. Atomistic Description of Thiostannate-Capped CdSe Nanocrystals: Retention of Four-Coordinate SnS4 Motif and Preservation of Cd-Rich Stoichiometry. *J. Am. Chem. Soc.* **2015**, *137* (5), 1862−1874.

(81) Prohaska, T.; Irrgeher, J.; Benefield, J.; Böhlke, J. K.; Chesson, L. A.; Coplen, T. B.; Ding, T.; Dunn, P. J. H.; Gröning, M.; Holden, N. E.; et al. Standard atomic weights of the elements 2021 (IUPAC Technical Report). *Pure Appl. Chem.* **2022**, *94* (5), 573−600.

(82) Nakamoto, K. Theory of Normal Vibrations. In *Infrared and Raman Spectra of Inorganic and Coordination Compounds*; John Wiley & Sons, Inc., 2008; pp 1−147.

(83) Lasia, A. The Origin of the Constant Phase Element. *J. Phys. Chem. Lett.* **2022**, *13* (2), 580−589.

(84) Brug, G. J.; Vandeneeden, A. L. G.; Sluyters-Rehbach, M.; Sluyters, J. H. The Analysis of Electrode Impedances Complicated by the Presence of a Constant Phase Element. *J. Electroanal. Chem.* **1984**, *176* (1−2), 275−295.

(85) Irvine, J. T. S.; Sinclair, D. C.; West, A. R. Electroceramics: Characterization by Impedance Spectroscopy. *Adv. Mater.* **1990**, *2* (3), 132−138.

(86) Muy, S.; Bachman, J. C.; Chang, H.-H.; Giordano, L.; Maglia, F.; Lupart, S.; Lamp, P.; Zeier, W. G.; Shao-Horn, Y. Lithium Conductivity and Meyer-Neldel Rule in Li3PO4−Li3VO4−Li4GeO4 Lithium Superionic Conductors. *Chem. Mater.* **2018**, *30* (16), 5573−5582.

(87) Zhou, L.; Zhang, Q.; Nazar, L. F. Li-Rich and Halide-Deficient Argyrodite Fast Ion Conductors. *Chem. Mater.* **2022**, *34* (21), 9634−9643.

(88) Plass, M. A.; Bette, S.; Philipp, N.; Moundrakovski, I.; Küster, K.; Dinnebier, R. E.; Lotsch, B. V. Influence of synthesis and substitution on the structure and ionic transport properties of lithium rare earth metal halides. *J. Mater. Chem. A* **2023**, *11* (24), 13027−13038.

(89) von Meyer, W.; Neldel, H. Über die Beziehungen zwischen der Energiekonstanten ε und der Mengenkonstanten a in der Leitwerts Temperaturformel bei oxydischen Halbleitern. *Z. Technol. Phys.* **1937**, *18*, 588.

(90) Gao, Y.; Li, N.; Wu, Y.; Yang, W.; Bo, S.-H. Rethinking the Design of Ionic Conductors Using Meyer−Neldel−Conductivity Plot. *Adv. Energy Mater.* **2021**, *11* (13), 2100325.

(91) *Le Système international d'unités/The International System of Units [Brochure]*; 2024.

(92) Culver, S. P.; Koerver, R.; Krauskopf, T.; Zeier, W. G. Designing Ionic Conductors: The Interplay between Structural Phenomena and Interfaces in Thiophosphate-Based Solid-State Batteries. *Chem. Mater.* **2018**, *30* (13), 4179−4192.

(93) Yang, H.; Wu, N. Q. Ionic conductivity and ion transport mechanisms of solid-state lithium-ion battery electrolytes: A review. *Energy Sci. Eng.* **2022**, *10* (5), 1643−1671.

(94) Li, S.; Lin, J.; Schaller, M.; Indris, S.; Zhang, X.; Brezesinski, T.; Nan, C.-W.; Wang, S.; Strauss, F. High-Entropy Lithium Argyrodite Solid Electrolytes Enabling Stable All-Solid-State Batteries. *Angew. Chem., Int. Ed.* **2023**, *62* (50), No. e202314155.